

ransport property of inhomogeneous strained graphene

Bing-Lan Wu(吴冰兰), Qiang Wei(魏强), Zhi-Qiang Zhang(张智强), and Hua Jiang(江华)
Citation: Chin. Phys. B, 2021, 30 (**3**): 030504. DOI: 10.1088/1674-1056/abe3e3
Journal homepage: http://cpb.iphy.ac.cn; http://iopscience.iop.org/cpb

What follows is a list of articles you may be interested in

Stable water droplets on composite structures formed by embedded water into fully hydroxylated *β*-cristobalite silica

Hanqi Gong(龚菡琪), Chonghai Qi(齐崇海), Junwei Yang(杨俊伟), Jige Chen(陈济舸), Xiaoling Lei(雷晓玲), Liang Zhao(赵亮), and Chunlei Wang(王春雷)
Chin. Phys. B, 2021, 30 (**1**): 010503. DOI: 10.1088/1674-1056/abc2b7

Topological Anderson insulator in two-dimensional non-Hermitian systems

Hongfang Liu(刘宏芳), Zixian Su(苏子贤), Zhi-Qiang Zhang(张智强), Hua Jiang(江华)
Chin. Phys. B, 2020, 29 (**5**): 050502. DOI: 10.1088/1674-1056/ab8201

Conservation laws for Birkhoffian systems of Herglotz type

Yi Zhang(张毅), Xue Tian(田雪)
Chin. Phys. B, 2018, 27 (**9**): 090502. DOI: 10.1088/1674-1056/27/9/090502

Nonlinear suboptimal tracking control of spacecraft approaching a tumbling target

Zhan-Peng Xu(许展鹏), Xiao-Qian Chen(陈小前), Yi-Yong Huang(黄奕勇), Yu-Zhu Bai(白玉铸), Wen Yao(姚雯)
Chin. Phys. B, 2018, 27 (**9**): 090501. DOI: 10.1088/1674-1056/27/9/090501

Chemical structure of grain-boundary layer in $SrTiO_3$ and its segregation-induced transition: A continuum interface approach

Hui Gu(顾辉)
Chin. Phys. B, 2018, 27 (**6**): 060503. DOI: 10.1088/1674-1056/27/6/060503

RAPID COMMUNICATION

Transport property of inhomogeneous strained graphene*

Bing-Lan Wu(吴冰兰)[1], Qiang Wei(魏强)[2], Zhi-Qiang Zhang(张智强)[1,†], and Hua Jiang(江华)[1,3,‡]

[1] School of Physics and Technology, Soochow University, Suzhou 215006, China
[2] State Key Laboratory of Quantum Optics and Quantum Optics Devices, Institute of Laser Spectroscopy, Shanxi University, Taiyuan 030006, China
[3] Institute for Advanced Study, Soochow University, Suzhou 215006, China

(Received 14 November 2020; revised manuscript received 1 January 2021; accepted manuscript online 7 February 2021)

In analogy to real magnetic field, the pseudo-magnetic field (PMF) induced by inhomogeneous strain can also form the Landau levels and edge states. In this paper, the transport properties of graphene under inhomogeneous strain are studied. We find that the Landau levels have non-zero group velocity, and construct one-dimensional conducting channels. In addition, the edge states and the Landau level states in PMF are both fragile under disorder. We also confirm that the backscattering of these states could be suppressed by applying a real magnetic filed (MF). Therefore, the transmission coefficient for each conducting channel can be manipulated by adjusting the MF strength, which indicates the application of switching devices.

Keywords: disorder effect, pseudo-magnetic field, strain, transport properties

PACS: 05.50.+q, 03.65.Vf **DOI:** 10.1088/1674-1056/abe3e3

1. Introduction

Over the past decades, the pseudo-magnetic field (PMF) attracts lots of attention due to the synthetic gauge field induced by the mechanical strain in materials,[1–4] which provides a new way of tailoring their electronic properties.[5–15] In graphene, for example, inhomogeneous strain can modulate the coordinate of Dirac cones which initially located at high-symmetry points K and K'.[1,2] Such inhomogeneous strain-induced pseudo-gauge field $\boldsymbol{A}_{\rm s}$ enters into the effective Dirac Hamiltonian $H = v_{\rm f}\boldsymbol{\sigma}\cdot\boldsymbol{p}$ by replacing the mechanical momentum $\boldsymbol{p}$ with the generalized momentum $\boldsymbol{p}\pm e\boldsymbol{A}_{\rm s}$, where $\pm$ denotes the K and K' valleys, respectively. In experiments, various inhomogeneous strained structures have been realized for graphene,[16–23] and the related PMF can reach up to hundreds of Teslas.[24,25]

The huge field strength also promotes many experimental groups to explore the PMF in artificial graphene systems.[26–28] Among them, the realization of PMF in phonon crystals is an important progress in recent years.[29–32] Especially, PMF induced Landau levels (LLs) and edge states are successfully achieved in such a system.[32] It is natural to ask whether these two states pose the similar transport properties to those in magnetic fields (MFs). As is known, in quantum Hall effect, the edge states introduced by the MFs (U(1) gauge field) are robust against disorder,[2,33–36] while the corresponding LLs are localized. However, the edge states and the LLs in PMF[29,37–43] should be different, since the time-reversal symmetry ensures that the effective PMF of K valley is opposite to that of K'. Therefore, the influence of disorder to states in PMF should be addressed.

In this paper, we study the transport properties of states in PMF. First, we construct an inhomogeneous strained graphene structure in which an uniform PMF is obtained. Then, the influence of disorder to LLs and edge states is numerically calculated. We find that the edge states induced by PMF are fragile to disorder. Furthermore, the dispersion of LL (except the zeroth LL) is tilted. It acts as one-dimensional channel inside the bulk, and disorder can also cause strong backscattering. We also find that the backscattering for both edge states and LL channels originating from PMF can be suppressed by an external MF,[40,44] because the spatial overlap between counter-propagating channels protected by time-reversal symmetry will be lifted. The above behaviors have the potential application in mesoscopic devices.

2. Strained graphene model and corresponding spectra

We consider a model with inhomogeneous strained graphene structure, as shown in Fig. 1(a). The tight-binding Hamiltonian reads[1,2]

$$H = \sum_i \varepsilon_i c_i^\dagger c_i + \sum_{\langle i,j\rangle} t_{ij}\, {\rm e}^{{\rm i}\int e\boldsymbol{A}\cdot{\rm d}\boldsymbol{l}/\hbar} c_i^\dagger c_j + {\rm h.c.}, \tag{1}$$

where c_i ($c_i^\dagger$) is the creation (annihilation) operator of site i. ε_i is the Anderson disorder[45,46] and satisfies the uniform distribution $[-W/2, W/2]$ with disorder strength W. $\boldsymbol{A}$ is the

*Project supported by the National Basic Research Program of China (Grant No. 2019YFA0308403) and the National Natural Science Foundation of China (Grant No. 11822407).

†Corresponding author. E-mail: zqzhang2018@stu.suda.edu.cn
‡Corresponding author. E-mail: jianghuaphy@suda.edu.cn

© 2021 Chinese Physical Society and IOP Publishing Ltd

vector potential of the MF $\boldsymbol{B} = (0,0,B)$, and $\mathrm{d}\boldsymbol{l}$ is the vector between i and j sites. The summation $\langle i,j\rangle$ runs over all the nearest-neighbor sites. For simplicity, the MF is in terms of the magnetic flux ϕ, where $\phi = 3\sqrt{3}a^2Be/4\hbar$.

To simulate the inhomogeneous stain-induced PMF, the hopping strength t_{ij} is simply classified into two categories.[40,47] First, the inhomogeneous strain-induced hopping in the vertical direction (y) is a linear function of the position y,

$$t_y = t\,(1+\alpha y)\,, \tag{2}$$

in which α (in units of a^{-1}, a is the lattice constant) is the parameter that characterizes the degree of strain. t is the energy unit. A typical distribution of t_y is plotted in Fig. 1(b). It shows the hopping strength marked in Fig. 1(a) by red dashed ellipses. Second, the hopping strength in the other two directions remains a constant $t_{ij} = t$ (see Appendix A). The effective Hamiltonian for K valley is written as[1]

$$H_K = \begin{pmatrix} 0 & v_x\,(p_x + eA_x) - \mathrm{i}v_y p_y \\ v_x\,(p_x + eA_x) + \mathrm{i}v_y p_y & 0 \end{pmatrix}, \tag{3}$$

where $v_x = (3-\alpha y)at/2\hbar$ and $v_y = 3(1+\alpha y)at/2\hbar$ are the Fermi velocities in the x and y directions, respectively (see Appendix B). p_x (p_y) is the momentum measured from the unstrained Dirac point (K). Thus, $\boldsymbol{A}_\mathrm{s} = (\frac{2\alpha y}{3a}, 0, 0)$ (in units of $\hbar/e$) [see Appendix B] is the pseudo-gauge potential that describes the effect of strain, and the PMF can be obtained by $\boldsymbol{B}_s = \nabla \times \boldsymbol{A}_\mathrm{s} = (0,0,B_\mathrm{s})$ with $B_\mathrm{s} = \frac{2\alpha}{3a}$. Furthermore, the sign of the pseudo-gauge field is opposite in K' valley (the gauge potential is $-\boldsymbol{A}_\mathrm{s}$ for K'), which ensures the overall time-reversal symmetry [see Fig. 5(b)]. As is known, the electronic structure of strained graphene ribbons strongly depends on the edge shape. Thus the shape of edge will also play roles in the strain effects. The above discussion is only applicable to zigzag edge, not armchair edge.[48]

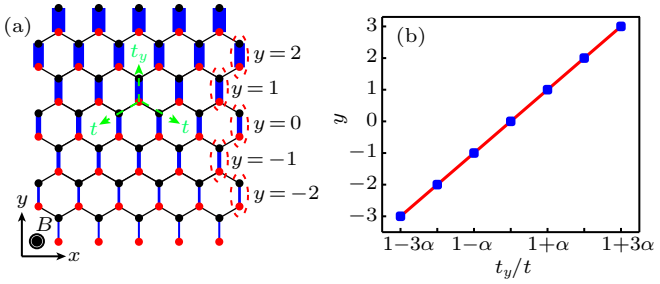


Fig. 1. (a) A realization of PMF in graphene. It is achieved by adjusting the hopping along y direction. The MF is along z direction, and the width of the solid lines implies the hopping strength. The dashed green arrows show the vertical hopping t_y and the rest of the hopping t. (b) A typical plot of t_y versus y for (a).

In order to quantitatively describe the properties of states in PMF, we study the transport in a two-terminal device for different conditions. The two-terminal differential conductance is $G = \mathrm{e}^2/hT_\mathrm{LR}$ with $T_\mathrm{LR} = \mathrm{Tr}[\Gamma_\mathrm{L}G^\mathrm{r}\Gamma_\mathrm{R}G^{r\dagger}]$, where $G^\mathrm{r} = [E_\mathrm{f} + \mathrm{i}0^+ - H - \Sigma_\mathrm{L}^\mathrm{r} - \Sigma_\mathrm{R}^\mathrm{r}]^{-1}$ is the retarded Green's function.[49,50] E_f is the Fermi energy, and H is the Hamiltonian of the central region. The line-width function is $\Gamma_\mathrm{L/R} = \mathrm{i}[\Sigma_\mathrm{L/R}^\mathrm{r} - \Sigma_\mathrm{L/R}^{r\dagger}]$, and $\Sigma_\mathrm{L/R}^\mathrm{r}$ is the self-energy of the leads L/R. In our numerical calculation, the size of the device is $\sqrt{3}N_x a/2 \times (3N_y - 2)a/4$. N_x and N_y are the lattice sites along x and y directions, respectively (It should be noted that the width of the system N_y is limited. The maximum value N_y can take is about 262). The current is along the x direction. In addition, the deformation parameter is fixed at $\alpha = 0.015$. G is averaged over 1000 disordered configurations.

3. Transport properties of edge states of strained graphene

In common view, topological edge states should be robust against disorder and lead to disspationless transport,[51–56] e.g., QH and QSH. Very recently, such guideline more or less motivates the discovery of 'QH' induced by PMF. Thus, we first investigate the transport properties of edge states under PMF in this section.

Figures 2(c) and 2(d) show the distribution of edge states with $E_\mathrm{f} = 0.016t$ [see the green and black dots in Figs. 2(a) and 2(b)]. Different from the edge states of QH systems, the counter-propagating states under PMF only exist around the $N_y = 202$ boundary, being consistent with previous studies.[29] It is noteworthy that the quality of edge states in this strained graphene depends on the ribbon width N_y and strain parameters α (see Appendix C). Since the spatial overlap will enhance backscattering between the counter-propagating states, one can anticipate that edge states in PMF would be fragile to disorder. Thus, we study the variation of differential conductance G for edge states under disorder. For simplicity, the Fermi energy is fixed at $E_\mathrm{f} = 0.016t$ with $\phi = 0$ (i.e., MF is absent), where only the edge states exist [see Fig. 2(a)]. When the disorder concentrates on the upper region of the sample [see Fig. 3(a)], we find that G decreases sharply even for weak disorder [see Fig. 3(c)]. In contrast, if disorder locates on the area without edge states, the $G = e^2/h$ plateau exists when $W < t$ [see Figs. 3(b) and 3(d)]. The behavior of G also suggests that the counter-propagating edge states under PMF distinguish from the helical edge states in QSH, since the latter are robust against nonmagnetic disorder.

We also find that the external magnetic field will significantly redistribute the edge states when ϕ is large enough. For example, we plot the band structure in Fig. 2(b) with $\phi = 0.012$, where the counter-propagating edge states become separated in space [see Figs. 2(c) and 2(d)]. The redistributed channels are robust under disorder, which implies that the external magnetic field can eliminate the backscattering of the sample. If the edge states induced by PMF are destroyed by disorder, the external magnetic field will rebuild the quantized differential conductance G. As shown in Figs. 3(c) and

3(d), G increases with the increase of ϕ and reaches the quantized value e^2/h again at $\phi = 0.016$. In practical application, since disorder inevitably exists and edge channels induced by PMF can be destroyed even under weak disorder ($W \ll t$), a switch device could be achieved by adjusting the magnetic field strength in a sample with PMF.

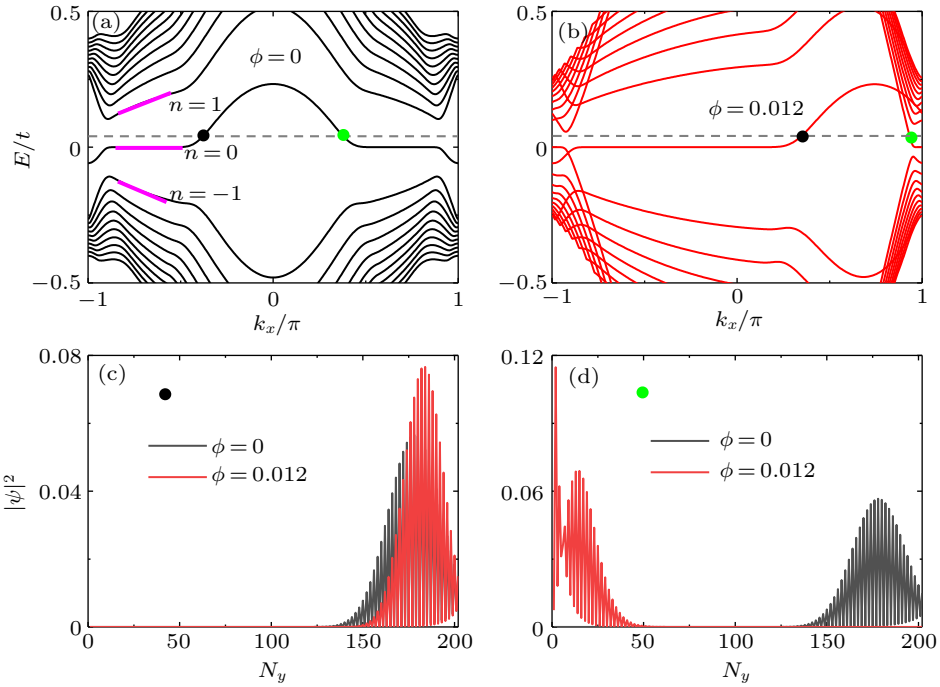


Fig. 2. (a) and (b) The energy spectra with the same strain parameters $\alpha = 0.015$, and the MFs are $\phi = 0$ and $\phi = 0.012$, respectively. (c) and (d) The probability density distributions for the edge states marked with black and green circles in panels (a) and (b).

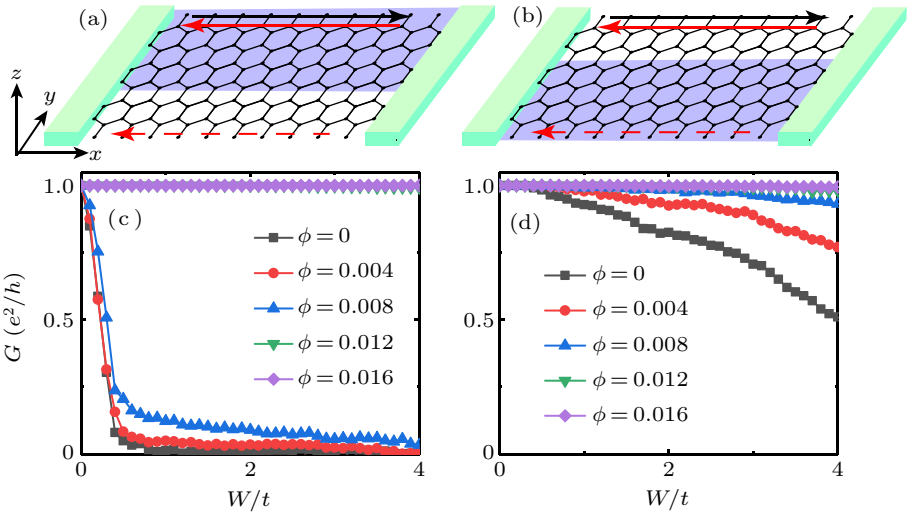


Fig. 3. (a) and (b) Schematic representation of two-terminal device (width $N_y = 202$, length $N_x = 100$), in which the violet region is disordered. The counter-propagating edge states are labeled with black and red arrows, where the left-moving edge states with and without ϕ are represented by solid red arrows and dotted red arrows, respectively. (c) and (d) Two-terminal differential conductance G versus disorder strength W for the devices shown in (a) and (b), respectively. The Fermi energy is fixed at $E_f = 0.016t$.

4. Transport properties of LLs of strained graphene

Interestingly, compared with the localized LLs in QHE, we find that LLs of strained graphene impose unique transport properties. Due to the uniform B_s, the energy spectrum in strained graphene is also quantized into discrete LLs

$$E_n \approx \mathrm{sign}(n)\sqrt{2e\hbar v_x v_y B_s |n|}. \tag{4}$$

Here, n is the LL index. Significantly, if $n \neq 0$, the LLs are no longer flat as it would be in an external MF, and thus it is more appropriate to call them pseudo-Landau levels (see Appendix D). For better comparison, we will still call them Landau levels (LLs). This is because both v_x , v_y and eigen-wavefunction[57]

$$\psi_{k_x}(y) \approx \frac{1}{\sqrt{2}} \begin{pmatrix} \varphi_{n-1}(y) \\ \pm\varphi_n(y) \end{pmatrix} \mathrm{e}^{\mathrm{i}k_x x} \tag{5}$$

(where $\varphi_n(y) = 2^{n/2} n! \, e^{-y^2/2} H_n(y)$, $H_n(y)$ is the Hermite polynomial of the n-th order) are y-dependent, thus $E_n(k_x)$ is not a constant but varies with k_x . For the sake of an intuitive picture, we return to the energy spectrum of a strained ribbon as shown in Fig. 2(a). The tilted LLs (except the zeroth LL) are observed as expected, and the tilted LLs indicate that the bulk states have non-zero group-velocity in the x direction. Therefore, LLs in PMF can transport electrons. Following, we pay attention to these LLs.

Figure 4(b) plots the spatial distribution of typical states for $n = -1$ LL with $E_f = -0.173t$ and $\phi = 0$ [i.e., the red and gray circles in Fig. 4(a)]. When MF is absent, the red and gray curves (corresponding to wavefunctions of forwarding LL and its counterpart) in Fig. 4(b) overlap due to the time-reversal symmetry, and the center of the wavefunction is located around $N_y = 100$. The effect of disorder on these states is also investigated. When Anderson disorder is applied to all areas of the device (i.e., both areas of A and B in Fig. 4(c)), differential conductance G decreases to zero for $W > 3t$ (see the red line in Fig. 4(d)), meaning all the states are localized by disorder. Then, we remove disorder in the range $N_y \in [50, 150]$ (i.e., yellow region A in Fig. 4(c)). G for such condition holds e^2/h plateau even when $W > 3t$ [see the black line in Fig. 4(d)]. These results imply that one channel still exists. According to Fig. 4(b), such conducting channel is corresponding to LL states. Moreover, the conducting LLs provide a routine to realize one-dimensional channels in a two-dimensional system, and one can manipulate the on/off status of these channels by adjusting the distribution of disorder.

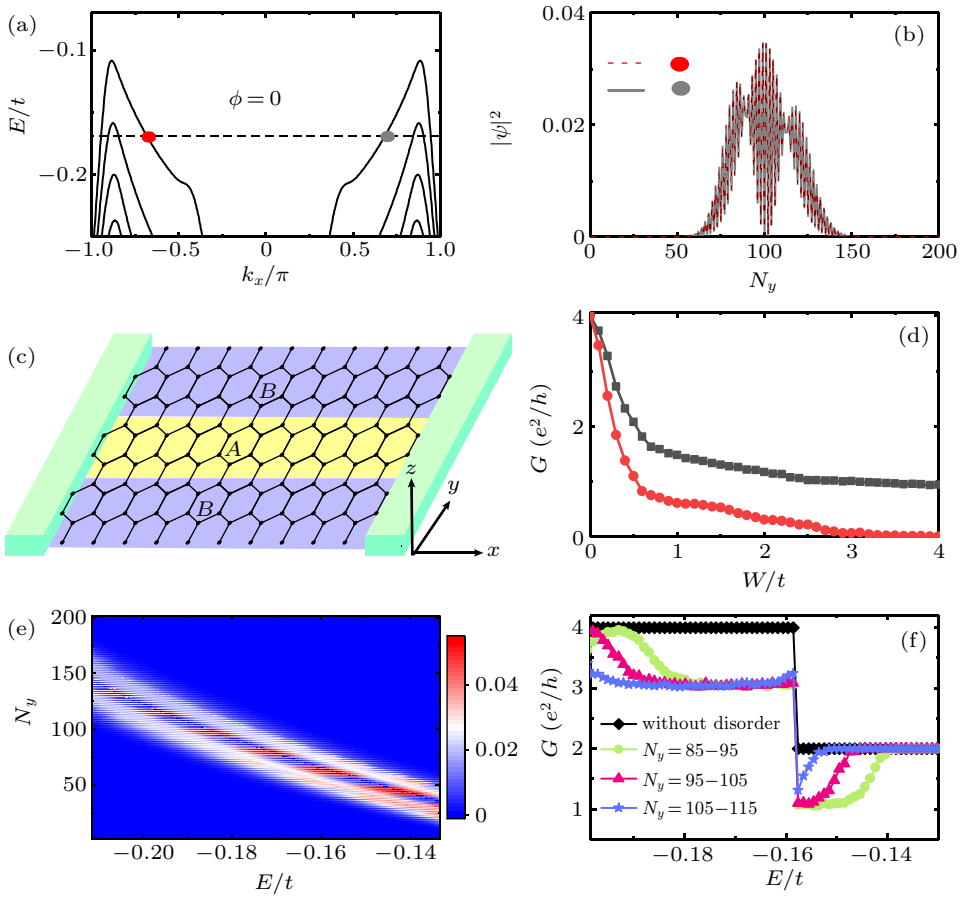


Fig. 4. (a) Energy spectrum of the strained graphene ribbon with $\alpha = 0.015$ and $N_y = 202$. The system holds time-reversal symmetry since the real MF $\phi = 0$. (b) The typical probability density distribution of counter-propagating bulk $n = -1$ LL states marked with the gray and red circles in panel (a) at $E_f = -0.0173t$. (c) Schematic of two-terminal device. The yellow region with width $\delta N_y = 10$ and two violet regions represent bulk disordered region A and edge disordered area B, respectively. (d) Differential conductance G versus disorder strength W at $E_f = -0.0173t$. (e) Probability density distributions $|\Psi|^2$ versus combinations (N_y , E) for all the bulk states in $n = -1$ LL. The color bar represents the probability density. (f) G for the device shown in panel (c) with the disordered region B shifting from $[85, 95]$ to $[105, 115]$. The disorder strength is fixed to $W = 4t$.

Although both edge states and LL states in PMF are one-dimensional channels, their energy dependent behaviors are totally different. The spatial distribution of edge states (LL states) is insensitive (sensitive) to E. To deeply understand the LL states, we present their distribution of wavefunction versus N_y and energy E for the $n = -1$ LL. As shown in Fig. 4(e), all the states of the LL are on the bulk of the sample. Also, the center of the wavefunction shifts almost linearly in space with an increase of E. These results are consistent with Eqs. (4) and (5) that the LLs ($n \neq 0$) are y (N_y) dependent. According to the above LLs behaviors, one can filter corresponding conducting channels for particular energy E region through engineering

the disorder distribution. As shown in Fig. 4(c), we put disorder only in region A. The differential conductance G decreases by e^2/h [see Fig. 4(f)], meaning that one of the bulk LL channels is filtered by the disorder. Moreover, the filtered energy region shifts to the lower energy as the disordered region A moves from $[85,95]$ to $[105,115]$. It agrees with the distribution of wavefunction for LLs [see Fig. 4(e)].

Finally, we fix the disorder distributed in the region $N_y \in [105,115]$ and study the effect of the MF. Figure 5(a) plots the band structure of graphene under both PMF and MF. As illustrated in Fig. 5(b), the combined contribution of MF (B) and PMF ($\pm B_s$) is that the electrons experience an effective magnetic field with strength $B \pm B_s$, where $\pm$ depends on the valley K/K'. Therefore, in consistence with Fig. 5(a), the energy of LLs ($E_n^{K/K'} \propto \mathrm{sign}(n)\sqrt{2v_x v_y |n(B \pm B_s)|}$) is obtained for K and K'. Due to MF B, a spatial overlap of counter-propagating LL channels protected by time-reversal symmetry will be lifted. Figure 5(c) plots the wavefunction distribution for $n=-1$ LL (correspond to the red and black circles in Fig. 5(a)). In contrast to the case of $\phi = 0$ [Fig. 4(b)], the spatial split of right and left moving LLs states is observed. This phenomenon originates from the fact that the external magnetic filed (B) shifts the $n=-1$ LL of the K valley to the lower energy ($E_K \propto -\sqrt{2v_x v_y |B+B_s|}$) and shifts the $n=-1$ LL of the K' valley to the higher energy ($E_{K'} \propto -\sqrt{2v_x v_y |B-B_s|}$). According to Eq. (4), the eigen-wavefunctions for $E = E_K$ and $E = E_{K'}$ are not overlapped. From Fig. 5(c), one can expected that the backscattering of LLs will be suppressed by MF. As shown in Fig. 5(d), in the absence of MF, the differential conductance G rapidly decreases by e^2/h because of the backscattering in the corresponding LL channels. However, once a real MF is added to the device, G increases obviously under the equivalent disorder strength W, and when the MF reaches $\phi = 0.003$, a quantized conductance plateau appears. Therefore, the MF controlled switching device can also be fabricated by using bulk LL in graphene with PMF.

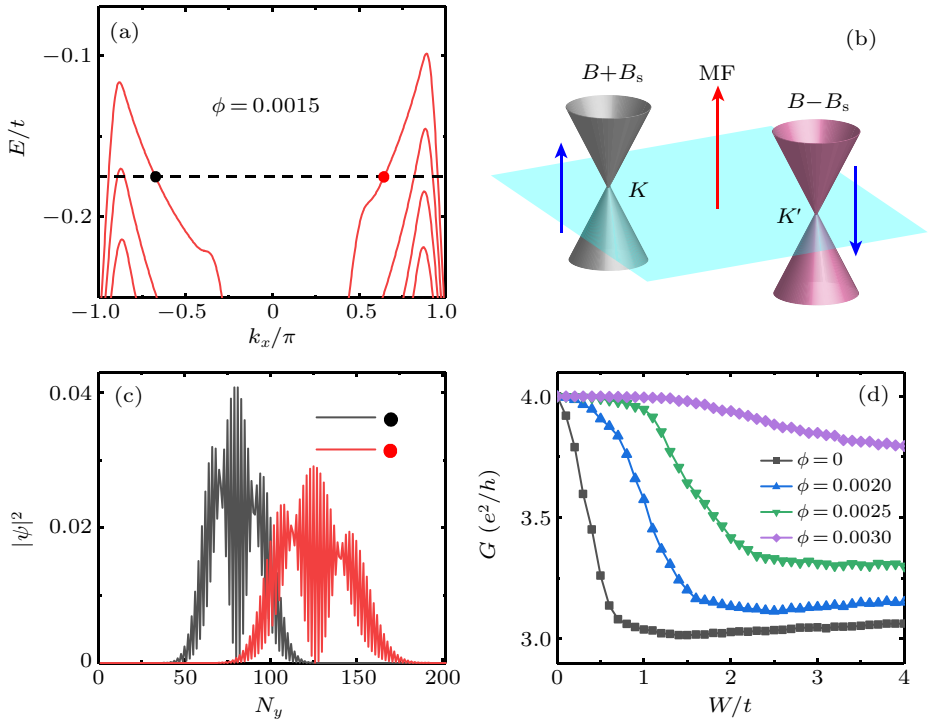


Fig. 5. (a) Energy spectrum of the strained graphene ribbon with $\alpha = 0.015$, $N_y = 202$, and the external magnetic field $\phi = 0.0015$. (b) Schematic diagram of effective magnetic field in K and K' valleys. The blue and red arrows represent the directions of the PMF and MF, respectively. (c) The probability density distribution of counter-propagating $n=-1$ LL states at $E_f = -0.0177t$ (the black and red circles in panel (a)). (d) G versus disorder strength W with the disorder distributing in the range $N_y \in [105,115]$ for different MF ϕ. Other parameters are the same as those in Fig. 2.

5. Conclusion

In summary, we study the transport properties of graphene states under inhomogeneous strain. We find both edge states and bulk LL states induced by pseudo-magnetic field build one-dimensional conducting channels, but they tend to be localized after the disorder is introduced. However, with the help of a real magnetic field, the suppression of backscattering recovers the conducting channels from localized LL states and edge states. Based on these results, a switching device could be realized in disordered pseudo-magnetic field graphene by adjusting the real magnetic field.

Acknowledgement

We are grateful to Chui-zhen Chen and Rui-Chun Xiao for helpful discussion.

Appendix A

When the uniaxial deformation is along an armchair direction (i.e., the y axis in the main text), the hopping strength $t_1(t_y)$, t_2, t_3 in all three directions will change. According to the equation given in Ref. [47], the hopping strengths t_2 and t_3 can be expressed as $t_2 = t_3 = (1+\alpha y)^{0.12} \approx 1+0.12\alpha y \approx 1$ when assuming $t_1 = 1+\alpha y$. In order to further clarify the appropriateness of the approximation $t_{2,3} \approx 1$, we plot the energy spectrum of strained graphene for $t_{2,3} = 1$ and $t_{2,3} = (1+\alpha y)^{0.12}$ in Fig. A1, and there is only little difference between the two models. Thus, our main results still hold. Besides, the hopping strength shown in our main text can be easily realized in artificial systems, [i.e., photonic crystals, electric circuits, etc.]. In our main text, we set $t_{2,3} = 1$ only for simplicity.

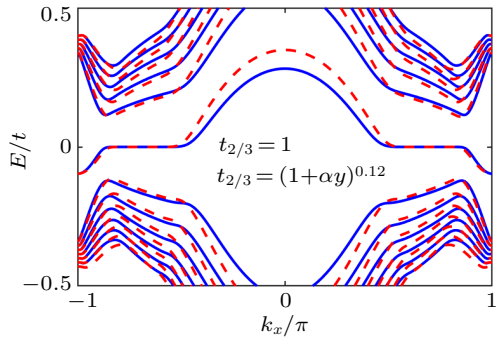


Fig. A1. Energy spectrum of the strained graphene for $t_{2,3} = 1$ (blue solid line) and $t_{2,3} = (1+\alpha y)^{0.12}$ (red dashed line).

Appendix B

In this appendix, we present the detailed derivation of the pseudo-gauge potential $\boldsymbol{A}$ and the Fermi velocity v_x, v_y in strained graphene. Since the results of K' valley are similar to those of K valley, we only consider the K valley for simplicity.

Based on the tight-binding approximation, the Hamiltonian of an unstrained graphene can be written as

$$H = \begin{pmatrix} 0 & h_{12} \\ h_{12}^* & 0 \end{pmatrix} = \begin{pmatrix} 0 & t_y + t\,\mathrm{e}^{\mathrm{i}\boldsymbol{k}\cdot\boldsymbol{a}_1} + t\,\mathrm{e}^{\mathrm{i}\boldsymbol{k}\cdot\boldsymbol{a}_2} \\ t_y + t\,\mathrm{e}^{-\mathrm{i}\boldsymbol{k}\cdot\boldsymbol{a}_1} + t\,\mathrm{e}^{-\mathrm{i}\boldsymbol{k}\cdot\boldsymbol{a}_2} & 0 \end{pmatrix}, \tag{B1}$$

in which $t_y = t$ and

$$\boldsymbol{a}_1 = \left(\frac{\sqrt{3}a}{2}, \frac{3a}{2}\right), \quad \boldsymbol{a}_2 = \left(-\frac{\sqrt{3}a}{2}, \frac{3a}{2}\right).$$

The corresponding Dirac point in K valley is sitting at

$$\boldsymbol{K}^{\mathrm{D}} = (K_x^{\mathrm{D}}, K_y^{\mathrm{D}}) = \left(\frac{4\pi}{3\sqrt{3}a}, 0\right),$$

which satisfies

$$h_{12} = t + 2t\cos\left(\frac{\sqrt{3}a}{2}K_x^{\mathrm{D}}\right) = 0. \tag{B2}$$

For the strained graphene, $t_y = t$ is replaced by $t_y = t(1+\alpha y)$. Thus, the Dirac point K is shifted from $\boldsymbol{K}^{\mathrm{D}}$ to $\boldsymbol{K}^{\mathrm{S}} = \boldsymbol{K}^{\mathrm{D}} + \boldsymbol{\delta}$, and the follow equation still holds:

$$h_{12} = t(1+\alpha y) + 2t\cos\left(\frac{\sqrt{3}a}{2}K_x^{\mathrm{S}}\right) = 0. \tag{B3}$$

Using $\boldsymbol{K}^{\mathrm{S}} = \boldsymbol{K}^{\mathrm{D}} + \boldsymbol{\delta}$, equation (B3) can be rewritten around the original Dirac point $\boldsymbol{K}^{\mathrm{D}}$ as

$$\begin{aligned} &t(1+\alpha y) + 2t\cos\left[\frac{\sqrt{3}a}{2}(K_x^{\mathrm{D}} + \delta_x)\right] = 0, \\ &t(1+\alpha y) + 2t\left[\cos\left(\frac{\sqrt{3}a}{2}K_x^{\mathrm{D}}\right)\right. \\ &\left. - \frac{\sqrt{3}a}{2}\sin\left(\frac{\sqrt{3}a}{2}K_x^{\mathrm{D}}\right)\delta_x\right] \approx 0, \end{aligned} \tag{B4}$$

where $\boldsymbol{\delta} = (\delta_x, 0, 0)$. We Taylor expand $\cos[\frac{\sqrt{3}a}{2}(K_x^{\mathrm{D}} + \delta_x)]$, because the strain induced shift of Dirac point δ_x is much smaller than $\boldsymbol{K}^{\mathrm{D}}$. According to Eq. (B2), the strain-induced pseudo-gauge potential along x direction is obtained as $A_x = \delta_x = \frac{2\alpha y}{3a}$. Thus, the pseudo-gauge potential is

$$\boldsymbol{A} = (\delta_x, 0, 0) = \left(\frac{2\alpha y}{3a}, 0, 0\right). \tag{B5}$$

To obtain the Fermi velocities v_x, v_y, we replace $\boldsymbol{k}$ by $\boldsymbol{K}^{\mathrm{S}} + \boldsymbol{\Delta}$. Then, the tight-binding Hamiltonian is given as follows:

$$\begin{aligned} h_{12} &= t(1+\alpha y) + 2t\cos\left[\frac{\sqrt{3}a}{2}(K_x^{\mathrm{S}} + \Delta_x)\right]\mathrm{e}^{\mathrm{i}\frac{3a}{2}\Delta_y} \\ &= t(1+\alpha y) + 2t\left[\cos\left(\frac{\sqrt{3}a}{2}K_x^{\mathrm{S}}\right)\cos\left(\frac{\sqrt{3}a}{2}\Delta_x\right)\right. \\ &\left. - \sin\left(\frac{\sqrt{3}a}{2}K_x^{\mathrm{S}}\right)\sin\left(\frac{\sqrt{3}a}{2}\Delta_x\right)\right]\mathrm{e}^{\mathrm{i}\frac{3a}{2}\Delta_y}, \end{aligned} \tag{B6}$$

in which $\boldsymbol{\Delta} = (\Delta_x, \Delta_y)$ is a vector between $\boldsymbol{K}^{\mathrm{S}}$ and $\boldsymbol{k}$. Moreover,

$$\begin{aligned} \cos\left(\frac{\sqrt{3}a}{2}K_x^{\mathrm{S}}\right) &= -\frac{1+\alpha y}{2}, \\ \sin\left(\frac{\sqrt{3}a}{2}K_x^{\mathrm{S}}\right) &= -\frac{\sqrt{3-2\alpha y-(\alpha y)^2}}{2} \end{aligned}$$

[see Eq. (B3)]. After Taylor expanding h_{12} to the first order, we find

$$h_{12} \approx -\mathrm{i}\frac{3at}{2}(1+\alpha y)\Delta_y - \frac{at}{2}(3-\alpha y)\Delta_x. \tag{B7}$$

Based on Eq. (B7), the Fermi velocities are

$$\begin{aligned} v_x &= \frac{at}{2\hbar}(3-\alpha y), \\ v_y &= \frac{3at}{2\hbar}(1+\alpha y). \end{aligned} \tag{B8}$$

Appendix C

In this appendix, we study the variation of the relative broadening of the edge state l/N_y with strain parameters α for two different system sizes $N_y = 202$ and $N_y = 162$, where l is the edge state broadening and N_y is the ribbon width.

It can be seen from Fig. C1 that the smaller the strain strength is, the wider the edge state is expanded. However, for the larger system, its relative expansion is still small. Therefore, in order to obtain high-quality edge states, a larger strain parameter is needed for systems with a smaller sample size.

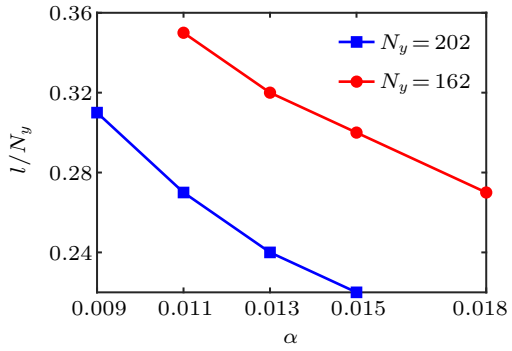


Fig. C1. The relative broadening of the edge state l/N_y for different strain parameters α, where the red and the blue lines correspond to the ribbon widths $N_y = 202$ and $N_y = 162$, respectively.

Appendix D

Unlike in a real magnetic field, the LLS formed in a PMF can be tilted. As shown in Fig. D1, the tilted bands (except states with zero energy) under PMF are obtained as expected, and all the states are on the bulk of the sample. Further, the corresponding edge states are also observed (see the inset near $N_y = 202$). Thus, these bands are similar to the traditional LLs in real magnetic fields, except the tilted dispersion. It is more appropriate to call them pseudo-Landau level (PLLs).

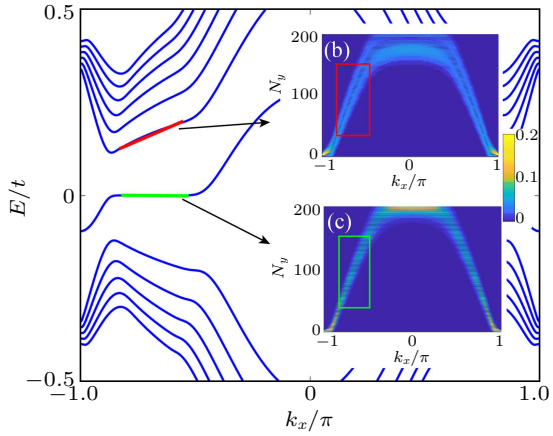


Fig. D1. (a) Energy spectrum of the strained graphene ribbon with $\alpha = 0.015$, $N_y = 202$. (b) and (c) Probability density distributions versus combinations (N_y, k_x) for all the states in the 1st and 0th energy levels, respectively. The states marked by the red and green lines in (a) correspond to the bulk states in the red and green boxes in (b) and (c), respectively.

References

[1] Vozmediano M A H, Katsnelson M I and Guinea F 2010 *Phys. Rep.* **496** 109
[2] Goerbig M O 2011 *Rev. Mod. Phys.* **83** 1193
[3] Manes J L, Juan F D, Sturla M and Vozmediano M A H 2013 *Phys. Rev. B* **87** 165131
[4] Kitt A L, Pereira V M, Swan A K and Goldberg B B 2012 *Phys. Rev. B* **85** 115432
[5] Guinea F, Katsnelson M I and Geim A K 2009 *Nat. Phys.* **6** 30
[6] Low T and Guinea F 2010 *Nano Lett.* **10** 3551
[7] Moldovan D, Masir M R and Peeters F M 2013 *Phys. Rev. B* **88** 035446
[8] Stegmann T and Szpak N 2016 *New J. Phys.* **18** 125422
[9] Carrillo-Bastos R, León C, Faria D, Latgé A, Andrei E Y and Sandler N 2016 *Phys. Rev. B* **94** 125422
[10] Torres V, Faria D and Latgé A 2018 *Phys. Rev. B* **97** 165429
[11] Zhai F, Ma Y and Chang K 2011 *New J. Phys.* **13** 083029
[12] Zhang D B, Seifert G and Chang K 2014 *Phys. Rev. Lett.* **112** 96805
[13] Jiang Y, Low T, Chang K, Katsnelson M I and Guinea F 2013 *Phys. Rev. Lett.* **110** 46601
[14] Wu Z, Zhai F, Peeters F M, Xu H and Chang K 2011 *Phys. Rev. Lett.* **106** 176802
[15] Chaves A, Covaci L, Rakhimov K yu, Farias G A and Peeters F M 2010 *Phys. Rev. B.* **82** 205430
[16] Georgiou T, Britnell L, Blake P, Gorbachev R V, Gholinia A, Geim A K, Casiraghi C and Novoselov K S 2011 *Appl. Phys. Lett.* **99** 93103
[17] Klimov N N, Jung S, Zhu S, Li T, Wright C A, Solares S D, Newell D B, Zhitenev N B and Stroscio J A 2012 *Science* **336** 1557
[18] Jang W J, Kim H, Shin Y R, Wang M, Jang S K, Kim M, Lee S, Kim S W, Song Y J and Kahng S J 2014 *Carbon* **74** 139
[19] Lim H, Jung J, Ruoff R S and Kim Y 2015 *Nat. Commun.* **6** 8601
[20] Yan H, Sun Y, He L, Nie J C and Chan M H W 2012 *Phys. Rev. B* **85** 35422
[21] Nemes-Incze P, Kukucska G, Koltai J, Kúrti J, Hwang C, Tapasztó L and Biró L P 2017 *Sci. Rep.* **7** 3035
[22] Neek-Amal M and Peeters F M 2012 *Phys. Rev. B* **85** 195445
[23] Neek-Amal M, Covaci L, Shakouri K and Peeters F M 2013 *Phys. Rev. B* **88** 115428
[24] Levy N, Burke S A, Meaker K L, Panlasigui M, Zettl A, Guinea F, Neto A H C and Crommie M F 2010 *Science* **329** 544
[25] Yeh N C, Teague M L, Yeom S, Standley B L, Wu R T P, Boyd D A and Bockrath M W 2011 *Surf. Sci.* **605** 1649
[26] Gomes K K, Mar W, Ko W, Guinea F and Manoharan H C 2012 *Nature* **483** 306
[27] Rechtsman M C, Zeuner J M, Tünnermann A, Nolte S, Segev M and Szameit A 2013 *Nat. Photon.* **7** 153
[28] Schomerus H and Halpern N Y 2013 *Phys. Rev. Lett.* **110** 13903
[29] Brendel C, Peano V, Painter O and Marquardt F 2017 *Bulletin of the American Physical Society* **2017**
[30] Abbaszadeh H, Souslov A, Paulose J, Schomerus H and Vitelli V 2017 *Phys. Rev. Lett.* **119** 195502
[31] Yang Z, Gao F, Yang Y and Zhang B 2017 *Phys. Rev. Lett.* **118** 194301
[32] Wen X, Qiu C, Qi Y, Ye L, Ke M, Zhang F and Liu Z 2019 *Nat. Phys.* **15** 352
[33] Thouless D J, Kohmoto M, Nightingale M P and Nijs M D 1982 *Phys. Rev. Lett.* **49** 41
[34] Klitzing K V, Dorda G and Pepper M 1980 *Phys. Rev. Lett.* **45** 494
[35] Zhang Y, Tan Y W, Stormer H L and Kim P 2005 *Nature* **438** 201
[36] Halperin B I 1982 *Phys. Rev. B* **25** 2185
[37] Mucha-Kruczynski M and Fal'ko V I 2012 *Solid State Commun.* **152** 1442
[38] Gradinar D A, Mucha-Kruczyński M, Schomerus H and Fal'Ko V I 2013 *Phys. Rev. Lett.* **110** 266801
[39] Settnes M, Leconte N, Barrios-Vargas J E, Jauho A P and Roche S 2016 *D Mater.* **3** 34005
[40] Roy B, Hu Z X and Yang K 2013 *Phys. Rev. B* **87** 121408
[41] Ghaemi P, Gopalakrishnan S and Ryu S 2013 *Phys. Rev. B* **87** 155422
[42] Costa D R da, Chaves A, Farias G A, Covaci L and Peeters F M 2012 *Phys. Rev. B* **86** 115434
[43] Mao J, Milovanović S P, Anđelković M, Lai X Y, Cao Y, Watanabe K, Taniguchi T, Covaci L, Peeters F M, and Geim A K 2020 *Nature* **584** 215

[44] Settnes M, Garcia J H and Roche S 2017 *2D Mater.* **4** 31006
[45] Anderson P W 1958 *Phys. Rev.* **109** 1492
[46] Abrahams E, Anderson P W, Licciardello D C and Ramakrishnan T V 1979 *Phys. Rev. Lett.* **42** 673
[47] Pereira V M, Castro Neto A H, Peres N M R 2008 *Phys. Rev. B.* **80** 045401
[48] For zigzag graphene, the K and K' valleys are well separated in momentum space. Thus, PMFs for these two valleys are $+B$ and $-B$, respectively. In contrast, for armchair graphene, both K and K' with opposite PMFs are folded into the Γ point, and the strong coupling of the two valleys greatly weaks the strain effect. Therefore, for armchair ribbons, the LLs and the chiral edge states will be formed by applying a real magnetic field, and the strain just tilt the LLs (except the zeroth LL) without affecting the properties of the edge state.
[49] Lewenkopf C H and Mucciolo E R 2013 *J. Comput. Electron.* **12** 203
[50] Datta S 1995 *Electronic transport in mesoscopic systems*, 2nd Edn.
[51] Hasan M Z and Kane C L 2010 *Rev. Mod. Phys.* **82** 3045
[52] Zhang H, Liu C, Qi X L, Dai X, Fang Z and Zhang S C 2009 *Nat. Phys.* **5** 438
[53] Qi X L and Zhang S C 2011 *Rev. Mod. Phys.* **83** 1057
[54] Chang C Z, Zhang J, Feng X, Shen J, Zhang Z, Guo M, Li K, Ou Y, Wei P, Wang L L, Ji Z Q, Feng Y, Ji S, Chen X, Jia J, Dai X, Fang Z, Zhang S C, He K, Wang Y, Lu L, Ma X C and Xue Q K 2013 *Science* **340** 167
[55] Schindler F, Cook A M, Vergniory M G, Wang Z, Parkin S S P, Bernevig B A and Neupert T 2018 *Sci. Adv.* **4** 6
[56] Jiang H, Wang L, Sun Q F and Xie X C 2009 *Phys. Rev. B* **80** 165316
[57] Faria D, León C, Lima L R F, Latgé A and Sandler N 2020 *Phys. Rev. B* **101** 81410